THE UNIVERSITY of EDINBURGH

Edinburgh Research Explorer

Structure-aware Dual-branch Network for Electrical Impedance Tomography in Cell Culture Imaging

Citation for published version:
Chen, Z & Yang, Y 2021, 'Structure-aware Dual-branch Network for Electrical Impedance Tomography in Cell Culture Imaging', *IEEE Transactions on Instrumentation and Measurement*, vol. 70, 4505409 . https://doi.org/10.1109/TIM.2021.3092524

Digital Object Identifier (DOI):
10.1109/TIM.2021.3092524

Link:
Link to publication record in Edinburgh Research Explorer

Document Version:
Peer reviewed version

Published In:
IEEE Transactions on Instrumentation and Measurement

General rights
Copyright for the publications made accessible via the Edinburgh Research Explorer is retained by the author(s) and / or other copyright owners and it is a condition of accessing these publications that users recognise and abide by the legal requirements associated with these rights.

Take down policy
The University of Edinburgh has made every reasonable effort to ensure that Edinburgh Research Explorer content complies with UK legislation. If you believe that the public display of this file breaches copyright please contact openaccess@ed.ac.uk providing details, and we will remove access to the work immediately and investigate your claim.

OPEN ACCESS

Download date: 17. May. 2022

Structure-aware Dual-branch Network for Electrical Impedance Tomography in Cell Culture Imaging

Zhou Chen, *Student Member, IEEE,* and Yunjie Yang, *Member, IEEE*

***Abstract*—lectrical Impedance Tomography (EIT) is an emerging imaging modality to monitor 3D cell culture dynamics through reconstructing the electrical properties of cell clusters.lectrical Impedance Tomography (EIT) is an emerging imaging modality to monitor 3D cell culture dynamics through reconstructing the electrical properties of cell clusters.E Recently, Machine Learning (ML) based approaches have achieved significant gains for the image reconstruction of EIT against conventional physical model based methods. However, continuous, multi-level conductivity distributions, which commonly exists in cell culture imaging, are more rigorous to reconstruct and remains challenging. This paper aims to tackle this challenge by proposing a structure-aware dual-branch deep learning method to predict both structure distribution and conductivity values. The proposed network comprises two independent branches to encode respectively the structure and conductivity features. The two branches are jointed later to make final predictions of conductivity distributions. Numerical and experimental evaluation results demonstrate the superior performance of the proposed method in dealing with the multi-level, continuous conductivity reconstruction problem.**

***Index Terms*—Deep learning, electrical impedance tomography, image reconstruction.**

I. Introduction

ELECTRICAL Impedance Tomography (EIT) has been extensively investigated over the last decades, on account of its intrinsic characteristics of non-destructiveness, low-cost fabrication, portability, non-ionizing radiation and real-time imaging capability. EIT reveals the internal conductivity distribution within the Region of Interest (ROI), and its sensing mechanism depends on a set of current injections followed by measuring the induced voltages on the boundary [1]. Compared to other tomographic imaging modalities, the advantageous properties of EIT have attracted increasing interests in diverse research areas, ranging from industrial process monitoring [2], [3] to biomedical imaging [4], [5]. In tissue engineering, non-destructive and label-free imaging and monitoring are demanding for the 3D cell culture process, where EIT has demonstrated its attractive potential with miniaturized sensors [5]–[7].

The major challenge of applying EIT for cell culture imaging lies in its highly nonlinear and ill-conditioned image reconstruction problem, leading to its susceptibility to distorted electric field lines and imperfect measurement data [8]. Majority of physical model based image reconstruction methods approximate the solution by minimizing least square errors and introducing a variety of regularization terms that encode prior information. Prevailing methods of this kind include, for instance, Tikhonov regularization [9], Total Variation (TV) regularization [10], sparsity regularization [11], Adaptive Group Sparsity (AGS) regularization [12], etc.

Despite the continuous advancement of the physical model based methods, it is still very difficult to accurately predict both the structure distribution and conductivity values, especially for the cases with multiple objects and different conductivity values, which commonly exist in cell culture processes. This essentially prevents EIT's transition from generating qualitative images to quantitative images. The emergence of machine learning has recently brought new possibility for high quality EIT image reconstruction. Some pioneering work includes [13] and its 3D version [14], which employed Sparse Bayesian Learning (SBL) and structure-aware priors to improve image quality. However, these works are based on the linearized EIT model and sparsity assumption, making it challenging to accurately estimate conductivity values and deal with non-sparse cases. Some other works [15]–[17] mapped directly from boundary voltage measurements to conductivity distributions, but focused on binary contrast reconstruction. The work in [18] adopted an UNet architecture [19] to remove aliasing artefacts from the TV results [10], but the network was trained using only hundreds of samples. Similarly, the Deep D-Bar approach [20] and the dominant-current deep learning scheme (DC-DLS) [21] used UNet to estimate the conductivity based on the approximated solution from different analytical methods. The DC-DLS is relatively time-consuming as the approximation is derived by an iterative algorithm. The induced-current learning method (ICLM) [22] was further proposed to resemble the inverse scattering problem. Our previous work [23] found the structure of target objects could be accurately estimated in the form of binary masks and facilitate distinguishing the conductivity contrast of multiple targets. However, the conductivity value still could not be precisely estimated due to the error introduced by the linearized EIT model. Accurate reconstruction of continuous, multi-level conductivity variations and the structural distribution remains very challenging.

In this paper, targeting at high-quality cell culture imaging, we propose a regression deep learning model to predict accurately both the geometric structure and conductivity value of multi-object, multi-level conductivity distributions. Inspired by multi-modal learning for activity and context recognition [24] and our previous work in [23], we develop a Structure-Aware Dual-Branch Network (SADB-Net) for EIT image reconstruction. The SADB-Net consists of two branches to

Z. Chen and Y. Yang are with the Intelligent Sensing, Analysis and Control Group, Institute for Digital Communications, School of Engineering, The University of Edinburgh, Edinburgh, UK, EH9 3JL (E-mail: y.yang@ed.ac.uk).

Manuscript received xx, 2021.

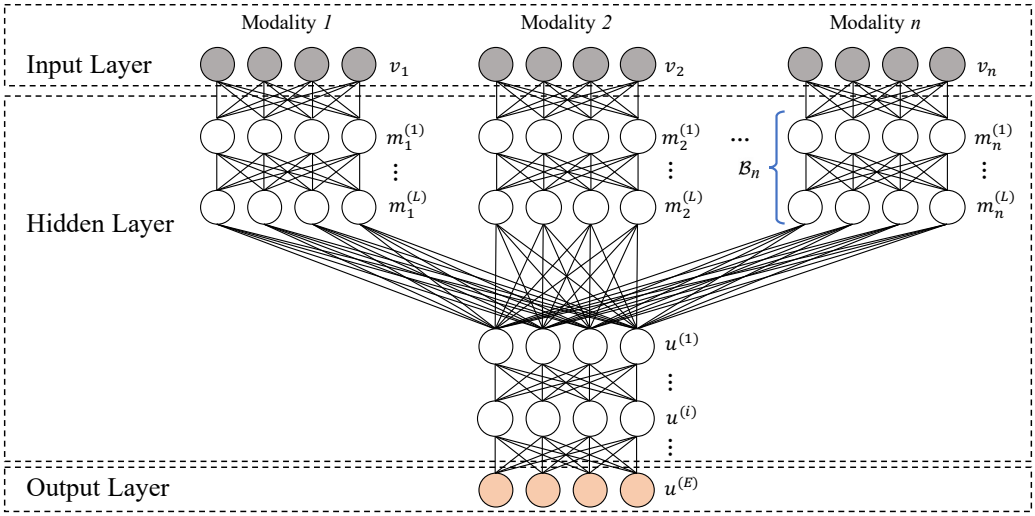

Fig. 1. Schematic illustration of generic modality-specific deep neural network.

learn respectively the structural and conductivity representations in the first place. Then, the multi-branch features are fused by two fully connected layers. We demonstrate the effectiveness of the SADB-Net in reconstructing continuous, multi-level conductivity distributions with both simulation and experimental data on MCF-7 breast cancer cell aggregates, and benchmark the results with the baseline and the state of the arts.

The remainder of this paper is organized as follows. Problem formation and SADB-Net are presented in Section II. Section III gives data generation and algorithm implementation details. Image reconstruction results based on simulation and experimental data are presented and discussed in Section IV. Finally, conclusions are drawn in Section V.

II. Methodology

A. Problem Formulation

The forward problem of EIT computes the boundary voltage $\mathbf{u}$ based on conductivity distribution $\boldsymbol{\sigma}$ within the ROI Ω, which can be most accurately described by the Complete Electrode Model (CEM) [25]. Let N be the number of electrodes attached at the boundary $\partial\Omega$, and n be the outward unit normal of $\partial\Omega$. With CEM, the potential $\mathbf{u}$ can be calculated using

$$\nabla \cdot (\boldsymbol{\sigma}\nabla\mathbf{u}) = 0, \quad x \in \Omega \tag{1}$$

$$\mathbf{u} + z_\ell \boldsymbol{\sigma}\frac{\partial \mathbf{u}}{\partial n} = U_\ell, \quad x \in e_\ell, \ell = 1, \ldots, N \tag{2}$$

$$\int_{e_\ell} \boldsymbol{\sigma}\frac{\partial \mathbf{u}}{\partial n} dS = I_\ell, \quad x \in e_\ell, \ell = 1, \ldots, N \tag{3}$$

$$\boldsymbol{\sigma}\frac{\partial \mathbf{u}}{\partial n} = 0, \quad x \in \partial\Omega \backslash \cup_{\ell=1}^{N} e_\ell \tag{4}$$

where e_ℓ represents the ℓth electrode; z_ℓ, I_ℓ, and U_ℓ denote respectively contact impedance, injected currents and corresponding potential on e_ℓ. The conservation of the charge and the choice of the reference point are added to CEM to further stabilize the solution $\mathbf{u}$, which are expressed as

$$\sum_{\ell=1}^{N} I_\ell = 0, \quad \sum_{\ell=1}^{N} U_\ell = 0. \tag{5}$$

The inverse problem of EIT aims to recover the conductivity distribution given the boundary voltage measurements. In this work, we solve the problem based on deep network parameterised by network weights $\boldsymbol{\theta}$, which is fed with the measurements and predicts the conductivity distribution.

B. Multi-Modal Deep Neural Network

We introduce the multi-branch characteristics of multi-modal deep learning to solve the target EIT-image-reconstruction problem. Some challenging learning tasks usually involve more than one sensing modalities providing diverse input data. In such cases, the multi-modal solutions fuse different sensing streams to boost the accuracy of the predicted results. Deep architectures, e.g. Restricted Boltzmann Machine (RBM) [26] and Convolutional Neural Network (CNN) [27], have been applied for multi-modal learning.

A straightforward strategy of multi-modal learning is to concatenate the inputs of different modalities, taking raw data or lightly pre-processed data at the input layer. Then the fused input is propagated through the neural network. However, this early fusion learning approach tends to emphasize the inherent cross-modality correlations [26], as early fusion and unbalanced mixture of inputs make it difficult to extract the potential intra-modality relations.

An alternative named Modality-specific Architecture (MA) [24] leverages both intra-modality and cross-modality correlations (see Fig. 1). In MA, information propagates through all layers. The input layer is fed with data from each modality and the output layer generates the final result. Separate branches ($\mathcal{B}_n$) are specified for each modality, without any connections in between. Through a couple of hidden layers in each branch, feature representations associated with each single modality

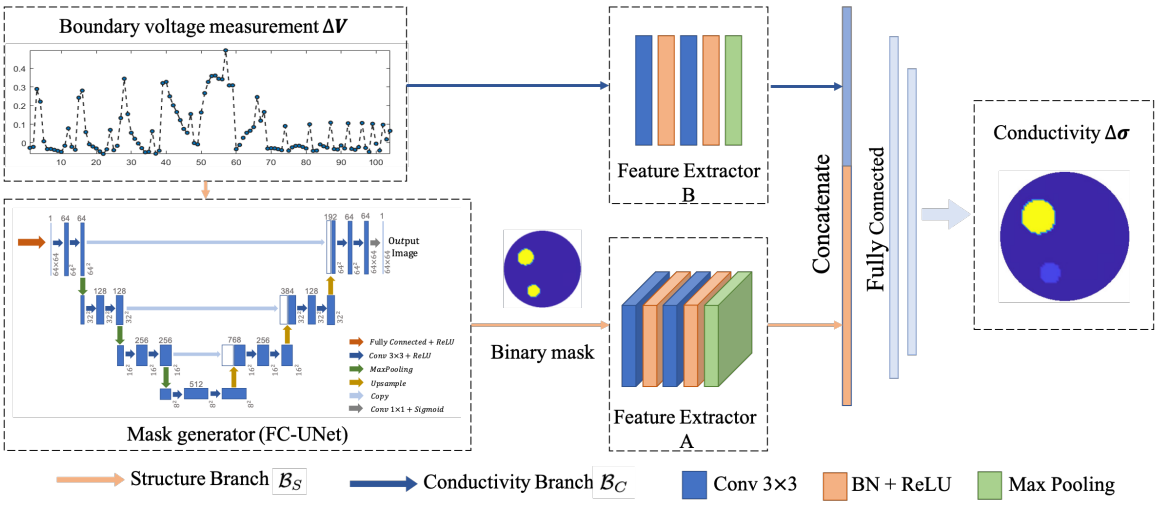

Fig. 2. Schematic illustration of the proposed Structure-aware Dual-branch Network (SADB-Net).

are learned and merged afterwards by subsequent layers $u^{(i)}$ in the network. The output neurons of the Lth hidden layer, i.e. $h_i^{(L)}$, are determined by every neuron in the previous layer, i.e. $h_j^{(L-1)}$. In general, it can be formulated as:

$$h_i^{(L)} = \gamma(\sum_j w_{ij}^{(L)} h_j^{(L-1)}) \tag{6}$$

where $w_{ij}^{(L)}$ denotes the unit weight connecting the jth neuron in layer $L-1$ with the ith neuron in layer L, and γ is the non-linear activation function. In this work, we simply adopt Rectified Linear Unit (ReLU) [28]:

$$\gamma(x) = \max(0, x). \tag{7}$$

The generic MA in Fig. 1 comprises a multi-layer perceptron, which can be replaced with a CNN for multi-modal learning. CNN is characterized by shared weights in form of stacks of filters, which parameters are trained to extract different high-level features. Using convolutional layers could avail more complicated patterns with far fewer parameters to learn. Inspired by MA, in this work we employ CNNs to learn intra-branch correlations over several layers and use fully connected layers to combine features from CNNs.

C. SADB-Net for EIT Image Reconstruction

We comprehend the EIT-image-reconstruction problem in a multi-modal context in the sense that the conductivity images reconstructed from the boundary voltage measurements generally contain two types of information: (a) geometric structure information and (b) conductivity value information. We first extract the binary structural information of the conductivity distribution and then utilize this binary image together with boundary voltage measurement as two inputs to tackle the regression problem. We will demonstrate this leads to more accurate estimation of both structure distribution and conductivity values. Fig. 2 shows the schematic illustration of the proposed Structure-Aware Dual-Branch Network (SADB-Net) for EIT image reconstruction based on this idea. We design two separate branches to deal with the two types of information: one is the structure related branch (see orange arrows in Fig. 2), and the other is conductivity-value related branch (see blue arrows in Fig. 2).

The structure branch $\mathcal{B}_S$ operates in the image domain, which consists of a mask generator and a feature extractor. The input vector first goes through the mask generator, which generates a binary mask to distinguish objects from the background. Following the work in [23], we use FC-UNet, a cascade of a fully connected layer and a UNet [19] to learn the mapping from boundary voltage measurement to a binary mask. A sigmoid activation function is selected as the last layer of FC-UNet to constrain all values within the range [0,1]. The feature extractor A is constructed by a standard CNN, where the stack of two convolutional layers with 3×3 kernels and padding of 1 are followed by a max pooling layer. A batch normalization layer and a ReLU activation layer are applied after each convolutional layer. In this step, the binary mask (64×64) is reduced to a feature map of size $16 \times 16 \times 16$ (height, width, channel) by the feature extractor.

The conductivity branch $\mathcal{B}_C$ takes the raw voltage measurement as input. Feature extractor B for $\mathcal{B}_C$ has exactly the same architecture as that for the branch $\mathcal{B}_S$, except that all layers operate in one dimension. The output is a 52×16 (length, channel) feature map.

The two feature maps learned from branches $\mathcal{B}_S$ and $\mathcal{B}_C$ are then concatenated together into a 4928-dimensional vector. This vector passes through two fully-connected layers, which fuse the information from the two branches. The first fully-connected layer encodes the vector down to a hidden feature with 4900 neurons. The second finally predicts conductivity distributions in a continuous manner. Each fully-connected layer is followed by a ReLU activation layer.

D. Loss Function

Let $\Delta\boldsymbol{\sigma} \in \mathbb{R}^n$ denote the conductivity variation distribution and $\Delta\mathbf{V} \in \mathbb{R}^m$ be the boundary voltage measurements change, which calculation is described in Section III-A2.

1) Binary Cross Entropy Loss ($\mathcal{L}_{BCE}$): For binary mask generation in $\mathcal{B}_S$, we explicitly train the FC-UNet parameterised by network weights $\boldsymbol{\theta}_{OD}$ using binary cross entropy loss on the predicted binary masks $\mathbf{M}_{pred} \in \mathbb{R}^n$, i.e.

$$\mathcal{L}_{BCE} = -\frac{1}{K}\sum_{i=1}^{K}(\mathbf{M}_{pred}^{(i)} \cdot log\mathbf{M}_{gt}^{(i)} + (1-\mathbf{M}_{pred}^{(i)}) \cdot log(1-\mathbf{M}_{gt}^{(i)})) \tag{8}$$

where K represents the size of dataset, $\mathbf{M}_{gt}^{(i)}$ denotes the ground truth for the ith input-target pair. Given the ground truth of conductivity distribution $\Delta\boldsymbol{\sigma}_{gt}^{(i)}$, $\mathbf{M}_{gt}^{(i)}$ is generated by setting all non-zero elements in $\Delta\boldsymbol{\sigma}_{gt}^{(i)}$ to one while the rest remains zero.

2) Total Loss ($\mathcal{L}_{Total}$): For the ultimate reconstruction task, our loss function intends to combine the per-pixel reconstruction accuracy with spatial piecewise smoothness in the predicted conductivity values.

Given the predicted conductivity distribution $\Delta\boldsymbol{\sigma}_{pred} = f_{mm-CNN}(\Delta\mathbf{V};\boldsymbol{\theta})$ and training dataset $\mathcal{D}$, we first define per-pixel losses with Mean Square Error (MSE), i.e.

$$\mathcal{L}_{MSE} = \frac{1}{K}\sum_{(\Delta\mathbf{V},\Delta\boldsymbol{\sigma}_{gt})\in\mathcal{D}} \|\Delta\boldsymbol{\sigma}_{gt} - \Delta\boldsymbol{\sigma}_{pred}\|^2 . \tag{9}$$

In addition to MSE loss, we also include l_2 loss (a regularization term) that is a function of the network weights $\boldsymbol{\theta}$:

$$\mathcal{L}_{l_2} = \|\boldsymbol{\theta}\|_2^2 = \sum_i |\boldsymbol{\theta}_i|^2. \tag{10}$$

Inspired by the work in super-resolution style transfer [29], the last loss term adopts the Total Variation (TV) loss $\mathcal{L}_{TV}$ as the piecewise smoothing penalty for $\Delta\boldsymbol{\sigma}_{pred}$, i.e.

$$\mathcal{L}_{TV} = \sum_{i,j\in\Omega} |\Delta\boldsymbol{\sigma}_{pred}(i+1,j) - \Delta\boldsymbol{\sigma}_{pred}(i,j)| + |\Delta\boldsymbol{\sigma}_{pred}(i,j+1) - \Delta\boldsymbol{\sigma}_{pred}(i,j)|. \tag{11}$$

The total loss $\mathcal{L}_{Total}$ is a combination of the above three terms:

$$\mathcal{L}_{Total} = \lambda_{MSE}\mathcal{L}_{MSE} + \lambda_{l_2}\mathcal{L}_{l_2} + \lambda_{TV}\mathcal{L}_{TV} \tag{12}$$

where $\lambda_{MSE}, \lambda_{l_2}, \lambda_{TV}$ are scalars for corresponding loss terms. Larger scalars are assigned to loss terms that are more critical. Here we consider the pixel-by-pixel loss $\mathcal{L}_{MSE}$ as the most critical term. The loss term scalars are determined by performing hyper-parameter searching on validation data set. After a series of experiments, we found that (1, 3e-6, 1e-8) is the most appropriate setting for $(\lambda_{MSE}, \lambda_{l_2}, \lambda_{TV})$.

E. Supervision Strategy

A specialized supervision strategy is developed as illustrated in Fig. 3. Inspired by multi-task deep learning [30], we first train the mask generator only with $\mathcal{L}_{BCE}$ for 100 epochs. Then we freeze all parameters of the object detector and train the remaining network with $\mathcal{L}_{Total}$ for around 200 epochs. That is, the full network is established on top of the pre-initialized mask generator.

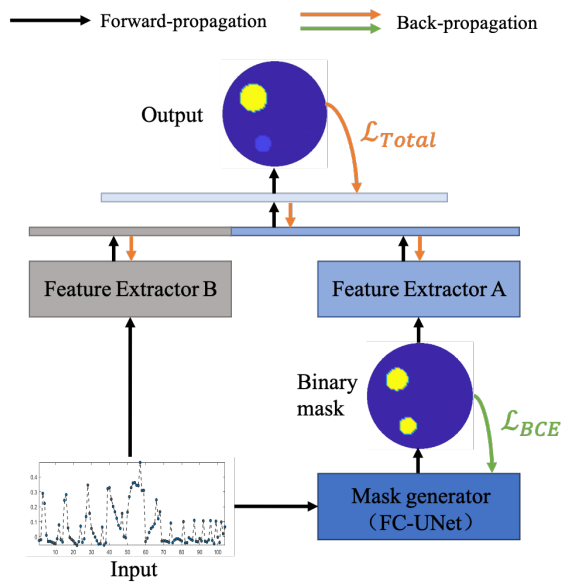

Fig. 3. Deep supervision of SADB-Net.

An easier way is to perform the end-to-end supervision by adding the binary cross entropy loss $\mathcal{L}_{BCE}$ to the total loss $\mathcal{L}_{Total}$ by imposing weighting factors. However, as the mask generator is closer to the input layer and away from the output layer, the gradients of the binary cross entropy loss become much smaller when they arrive at the object detector during back-propagation. Consequently, it requires much longer training time and is more likely to converge to a worse local minimum. In contrast, the proposed training strategy directly feeds $\mathcal{L}_{BCE}$ to the mask generator, which has two advantages: first, the mask generator is more sensitive to gradients from $\mathcal{L}_{BCE}$ during training; second, it facilitates faster and better convergence performance.

F. Evaluation Metrics

We adopt the commonly used Relative Image Error (*RIE*) to assess the quality of the reconstructed images, i.e.

$$RIE = \frac{||\Delta\boldsymbol{\sigma}_{pred} - \Delta\boldsymbol{\sigma}_{gt}||}{||\Delta\boldsymbol{\sigma}_{gt}||} \times 100\% \tag{13}$$

where $\Delta\boldsymbol{\sigma}_{pred}$ and $\Delta\boldsymbol{\sigma}_{gt}$ represent respectively the predicted and ground truth of conductivity distribution. *RIE* indicates the overall accuracy of the reconstruction quality in a pixel-by-pixel manner. Smaller *RIE* suggests better image quality.

III. Experimental Setup

A. Training Data Generation

To date, no open source EIT data set is available. Therefore, to mimic cell culture phantoms, we established an EIT dataset containing multiple continuously varying conductivity levels by modeling a circular 16-electrode EIT sensor in COMSOL Multiphysics (see Fig. 4(a)). The background conductivity is set as 0.05 $S{\cdot}m^{-1}$ and the conductivity of circular inclusions is randomly selected within the range [1e-4, 0.05) $S{\cdot}m^{-1}$. Apart

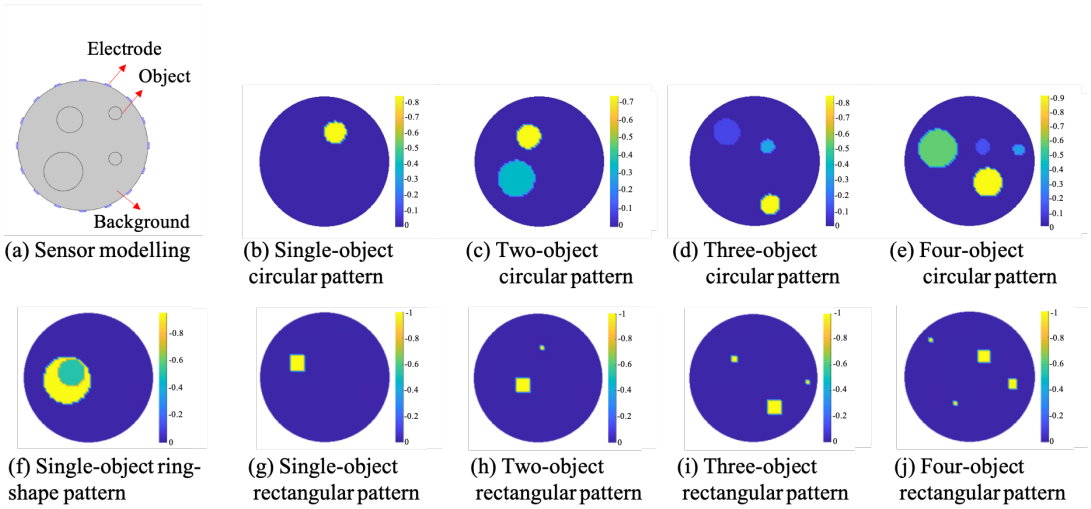

Fig. 4. Sensor modelling and examples of nine patterns in the EIT data set.

from uniformly distributed circular targets, we also evaluated the performance of phantoms with single ring-shaped objects. We generated another group of ring-shaped dataset. Within each circular object, a smaller circular region is randomly created with the conductivity of 1 $S \cdot m^{-1}$. The conductivity of the rest part of each object and the background is 0.1 and 2 $S \cdot m^{-1}$, respectively. To evaluate the performance of non-circular imaging targets, we established another dataset containing 1 to 4 rectangular inclusions. The conductivity of each rectangular inclusion and the background are 0.0001 and 0.05 $S \cdot m^{-1}$, respectively. We adopt adjacent measurement strategy [31] and a completed non-redundant measurement vector contains 104 values. Further, we divide the circular sensing region by a 64×64 quadrate mesh, which contains 3228 pixels.

In total, we randomly generated 54,333 pairs of samples through finite element modelling simulation. The data set consists of nine different patterns with random object sizes, positions and conductivity values (see examples in Fig. 4). This data set is further partitioned into training set (6k samples of each circular pattern, 4k samples of ring-shape pattern, 4k samples of each rectangular pattern), validation set (500 samples of each pattern), and testing set (all the remaining samples). Accordingly, the three subsets contain 44k, 4,500 and 5,833 samples, respectively.

1) Data Augmentation: We implement data augmentation by adding noise with diverse levels to voltage measurements in training, validation and testing data sets. The purpose is to mitigate the data limitation issue and improve robustness when dealing with noise-contaminated data. For the training and validation set, white noise with Signal-to-Noise Ratio (SNR) of 50dB and 40dB is added to half samples of each subset and the other half samples, respectively. The number of samples in training and validation subset is then doubled. In addition, we add white noise with SNR of 50dB and 40dB to all samples in the testing subset to validate the performance of SADB-Net. Table I gives the number of samples in training, validation, and testing subsets before and after augmentation.

TABLE I
NUMBER OF SAMPLES IN EACH DATA SET

Dataset	*Training*	*Validation*	*Testing*
Before Augmentation	44,000	4,500	5,833
After Augmentation	88,000	9,000	17,499

2) Data Normalization: To reduce systematic defect caused by sensor imperfection, an additional pre-processing procedure is conducted to normalize the voltage measurements and conductivity in the data set. Let $\boldsymbol{\sigma}_{ref}$ and $\mathbf{V}_{ref}$ represent respectively the conductivity distribution and corresponding voltage measurement when only background substance is present; $\boldsymbol{\sigma}_{mea}$ and $\mathbf{V}_{mea}$ denote respectively the conductivity distribution and voltage measurement after perturbations are present in the ROI. We normalize the voltage measurement and conductivity distribution in the following way:

$$\Delta \mathbf{V} = \frac{\mathbf{V}_{mea} - \mathbf{V}_{ref}}{\mathbf{V}_{ref}}, \tag{14}$$

$$\Delta \boldsymbol{\sigma} = \frac{\boldsymbol{\sigma}_{mea} - \boldsymbol{\sigma}_{ref}}{\boldsymbol{\sigma}_{ref}}. \tag{15}$$

B. Network Training

To train the FC-UNet as mask generator, the optimization setup is exactly the same as that in previous work [23]. For the rest of the SADB-Net, we use Adam [32] with a batch size of 25 and a base learning rate of 0.0001, which is reduced by a factor of 0.1 with a step size of 25. Except the pre-trained weights of FC-UNet, all other weights are initialized randomly. The weight decay in Adam has the same function with the l_2 penalty and thus is set as 3e-6. Training was carried out on two NVIDIA P5000 GPUs, and we select the model with the least validation loss as the final one to avoid overfitting.

C. Baseline

We select FC-UNet reported in [23] as the baseline algorithm since it does not require further preprocessing of the data set. As this paper tends to solve a regression problem, we replace the last sigmoid layer (suited for classification/segmentation) in the original FC-UNet with a ReLU layer.

We also compare performance with L1 regularization (L1) [11], Laplacian filter (Lap) [35], Sparse Bayesian Learning (SBL) [13] and LeNet [15]. L1 [11] is an iterative model-based reconstruction algorithm with maximum iteration number of 50. Lap is the one-step linear Gauss-Newton solver with Laplacian filter with a regularization factor of 0.05 [35]. LeNet [15] and SBL [13] are two recently reported learning-based EIT image reconstruction algorithms. SBL was implemented according to [13], where we select the stopping tolerance to be $1e-9$, the maximum iteration number to be 20 and the block size to be 7, after a careful tuning process.

IV. Results and Discussions

A. Evaluation on Simulation Data

1) Case Study: We show some representative reconstruction examples using testing data under 50dB SNR (see Fig. 5). Fig. 6 gives the RIE of each phantom.

Overall, SADB-Net outperforms the other five methods. L1, Lap, SBL, LeNet and the baseline are suboptimal because the Lap, LeNet and baseline contain artifacts, L1 and SBL keep underestimating the shape of the objects (see Fig. 5). In Phantom 1 and 2, only SADB-Net manages to recover all objects in terms of both shape and conductivity value. SADB-Net uses an extra pipeline to learn the conductivity value, merges this feature with the structural feature from the other pipeline, and could better recover the global information. In these cases, L1, Lap, SBL, LeNet and the baseline are unable to reveal the conductivity difference of the objects, whereas SADB-Net succeeds to reconstruct this critical information. Regarding the more challenging Phantom 3, L1, Lap, SBL and LeNet even fail to recognize the correct number of objects within the region and the baseline hardly distinguishes the two objects in the middle, not to mention the conductivity levels. However, SADB-Net recovers the best structural information and at least figures out the conductivity value of the one at lower left corner that is most significantly different from the background. For non-uniformly distributed inclusions, the reconstruction results demonstrate that all networks can handle Phantom 4 and 5 better than L1, Lap, and SBL especially in terms of shape reconstruction. The baseline is comparable to SADB-Net but SADB-Net can better localize the region with a lower conductivity contrast. Comparing the reconstruction results of Phantom 6, it is obvious that only SADB-Net provides the most accurate shape while the other methods tend to generate unexpected circular objects.

However, a remarkable advantage of the baseline can be noted, i.e. its shallower architecture with a straight pipeline is more sensitive to $\mathcal{L}_{TV}$ so that the reconstructed results are smoother than those of SADB-Net. The multi-branch representations which are joint later in SADB-Net are more informative, which consequently improves the overall image quality in terms of conductivity values of multiple objects, at the expense of less smoothness in the reconstructed images.

In Fig. 6, RIE of all methods in general get worse as the number of objects increases. SADB-Net consistently yields the best RIE of 27.73%, 41.61%, and 69.76% relatively for Phantom 1-3, suggesting its high accuracy of estimating complicated conductivity distributions. The gap among L1, Lap, SBL, LeNet and baseline shrinks with increasing inclusions. For ring targets in Phantom 4 and 5 and rectangular targets in Phantom 6, deep learning methods show significantly lower RIE than conventional methods.

Fig. 7 presents high- and low-contrast profiles of reconstructions for Phantom 1 and 2, marked by dashed line segments in the first row of Fig. 5. For the high-contrast case, L1, Lap, SBL and LeNet deviates far from the ground truth, while the baseline and SADB-Net can smooth the details but SADB-Net better follows the two transitions. With respect to the low-contrast profile, L1 and SADB-Net overlaps with the ground truth, but Lap, LeNet and baseline show deep troughs, suggesting obvious artefacts in their reconstructed background.

2) Quantitative comparisons: Table II reports the statistical average of *RIE* and running speed over all the testing data. We partition the results based on four different patterns in Fig. 4 and three noise levels, i.e. *noise free*, *50dB*, and *40dB*.

Similar to the trend in Fig. 6, all methods show degraded performance with increasing number of objects in the ROI, as it becomes more challenging to reconstruct. Fig. 8 further evaluates the performance of the given approaches under a wide range of SNR levels from 30dB to 70dB. It suggests all methods are generally robust to noise, with deep learning based methods, i.e. LeNet, baseline and SADB-Net, yielding much better *RIE* than conventional methods. Overall, SADB-Net performs the best in terms of *RIE*. This implies that learning the structure- and conductivity-related information with separate branches helps effectively to discriminate conductivity levels among inclusions, compared with concatenated learning with simple network architectures.

In terms of the reconstruction time, we compute the average running time of all the given algorithms on all cases in the testing data set, which is a conventional approach as adopted in [36]. Deep learning based approaches achieve high quality image reconstruction results at a very fast speed, approximately 50 times faster than L1, 600 times faster than Lap, 10,000 times faster than SBL. The LeNet consistently runs slightly faster than SADB-Net by 1.64ms, as it has a shallower structure, which costs slightly less computation for inferences. Nevertheless, the execution time of SADB-Net (below 2ms) is sufficiently good for implementing real-time EIT imaging.

B. Evaluation on Experimental Data

In addition to simulation study, we carried out real-world experiments on different miniature EIT sensors to examine the generalization ability of the proposed method. Image reconstruction on miniature EIT sensors is challenging due to its weak measurement signals and sensitivity to sensor imperfection. The miniature EIT sensor [33] (see Fig. 9(a))

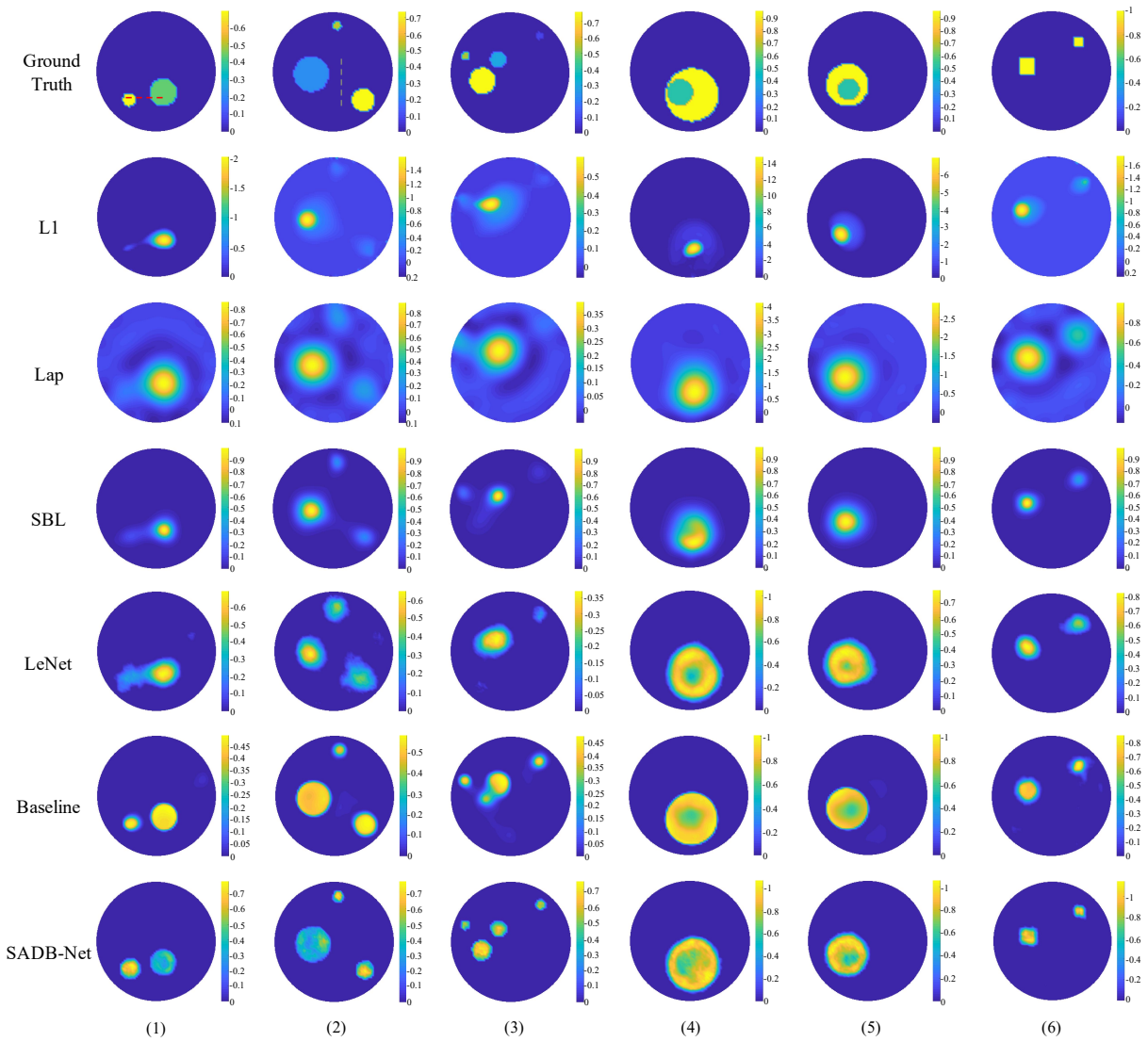

Fig. 5. Image reconstruction results based on simulation data (SNR = 50 dB) in testing set. Each column corresponds to a phantom.

TABLE II
PERFORMANCE COMPARISONS (*RIE* AND SPEED) UNDER DIFFERENT PHANTOM PATTERNS AND NOISE LEVELS.

No. of Objects	*Noise Free*				*50dB*				*40dB*			
	1	2	3	4	1	2	3	4	1	2	3	4
RIE (*L1* [11]) (%)	95.73	111.9	118.6	116.9	96.29	111.9	118.8	117.3	96.76	112.4	119.5	117.1
RIE (*Lap* [35]) (%)	87.31	104.3	111.6	110.1	87.43	104.6	111.7	111.5	87.61	104.8	111.6	111.7
RIE (*SBL* [13]) (%)	77.95	80.74	83.68	84.29	77.19	80.22	83.55	84.30	78.26	79.21	83.04	84.01
RIE (*LeNet* [15]) (%)	62.62	75.76	78.50	82.71	62.83	75.98	78.55	82.99	65.32	77.48	79.87	83.88
RIE (*Baseline* [16]) (%)	49.65	62.11	65.71	73.73	58.60	65.61	70.53	77.04	64.24	73.49	76.96	82.03
RIE (*SADB-Net*) (%)	**32.40**	**59.28**	**62.99**	**72.43**	**53.28**	**60.61**	**66.18**	**74.91**	**59.08**	**56.71**	**72.64**	**81.01**
Speed (*L1* [11]) (s)	0.05				0.05				0.05			
Speed (*Lap* [35]) (s)	0.59				0.60				0.59			
Speed (*SBL* [13]) (s)	12.63				13.09				12.91			
Speed (*LeNet* [15]) (s)	**0.22e-3**				**0.26e-3**				**0.25e-3**			
Speed (*Baseline* [16]) (s)	**1.08e-3**				**1.08e-3**				**1.09e-3**			
Speed (*SADB-Net*) (s)	**1.83e-3**				**1.91e-3**				**1.92e-3**			

Best results are highlighted in bold. Speed computes average model execution time per image.

is equipped with 16 planar electrodes at the substrate and the inner diameter of the sensing chamber is 15 mm. We use cucumber, carrot, and potato cylinders with similar size but different conductivity values as imaging targets. The background substance is saline with a conductivity of 0.25 $S \cdot m^{-1}$. The excitation frequency is 20kHz. We also examined

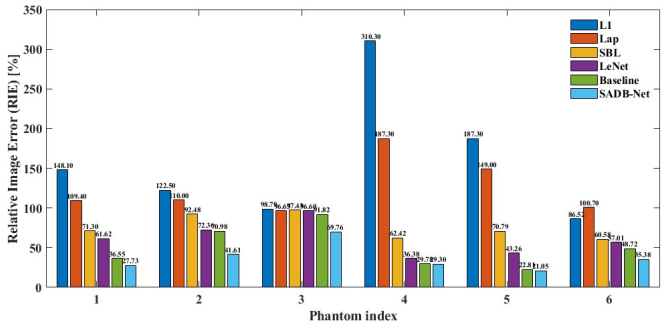

Fig. 6. Numerical comparisons of six phantoms based on *RIE*.

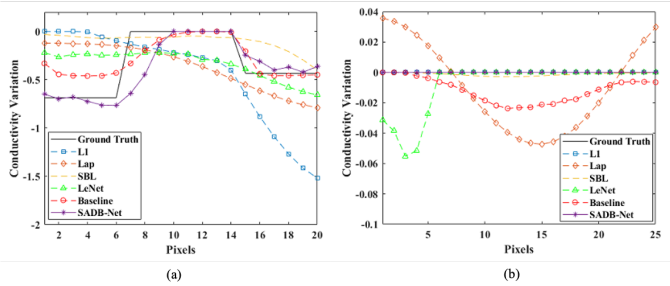

Fig. 7. (a) High-contrast profile in (3) of Fig. 5 and (b) low-contrast profile in (4) of Fig. 5.

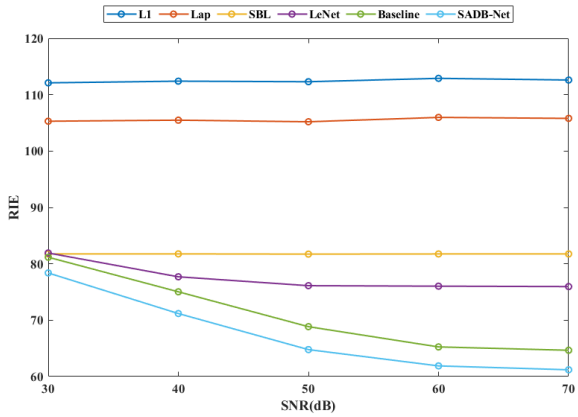

Fig. 8. Noise robustness comparison in terms of *RIE*.

the performance of the given methods on MCF-7 human breast cancer cell spheroids with a quasi-2D miniature EIT sensor [37], which has a diameter of 14mm. The two MCF-7 human breast cancer cell spheroids with a diameter of 2mm are less conductive than the background substance. The parameter setting for all methods is the same as in simulation.

Fig. 9 illustrates image reconstruction results of four phantoms. In experiment phantom 1, carrot has higher conductivity than cucumber, but both are lower than that of the background substance [34]. SBL could roughly recover such conductivity contrast but severely underestimates the size of both objects due to its strong sparsity constraint. Whilst L1, Lap, and LeNet could recover the shape of each object much better, but all generate significant artifacts (also can be found in simulations). The baseline even fails to tell either conductivity contrast or the target shape. SADB-Net performs better in terms of target shape and noise reduction, whilst hardly reconstruct the conductivity contrast. In experiment phantom 2, potato on the bottom-left corner induces a larger negative conductivity change than carrot on the top-right corner [34]. We can explicitly observe that L1 could hardly recover the top-right carrot cylinder, Lap suffers from significant artifacts, SBL underestimates target sizes, LeNet and the baseline are unable to reconstruct the conductivity contrast. Differently, SADB-Net demonstrates consistent performance outperforming the other approaches in terms of shape preservation, conductivity contrast prediction and noise reduction. Based on Eq. (15) and the measured conductivity of carrot, potato and cucumber in [34], we could deduct the relative conductivity changes of carrot, potato and cucumber under 20kHz are around -0.56, -0.76 and -0.81. By comparing the reconstructed images for experimental phantom 1 and phantom 2, we further confirm SADB-Net could better estimate both the conductivity change and the shape of imaging objects. Experiment phantom 3 and 4 contain two cell spheroids. L1, Lap, SBL and LeNet suffer from significant artifacts. They exhibit poor ability to distinguish the adjacent cell aggregates. SADB-Net yields consistently better shapes than the baseline. These results suggest that SADB-Net is able to generalize well to the real experimental setups. Additionally, the unique architecture of SADB-Net makes a worthwhile contribution to accurate predictions on not only structure but the conductivity difference in between objects.

V. Conclusion

We attempt to tackle the challenge of accurate reconstruction of the multi-object, multi-value conductivity distributions with EIT for tissue engineering applications. Typical convolutional networks (LeNet and the baseline model) run much faster than conventional approaches but are still unsatisfactory when estimating conductivity values. We proposed a novel network SADB-Net and demonstrated that:

1) by separating the estimation of structure distribution and conductivity values using two branches and then fusing the information together, SADB-Net could generate high-quality reconstructions of multi-object, multi-value distributions with better structural and conductivity estimation;
2) SADB-Net exhibits good generalization ability based on the experimental results on miniature EIT sensors.

In future work, we will apply the proposed approach in imaging dynamic 3D cell culture processes in tissue engineering. We also aim to extend this method to solve the 3-D EIT image reconstruction problem and apply it to image the in vitro 3D disease models in real time.

References

[1] R. H. Bayford, "Bioimpedance tomography (electrical impedance tomography)," *Annu. Rev. Biomed. Eng.*, vol. 8, pp. 63–91, Aug. 2006.
[2] W. Wang, *Industrial Tomography: Systems and Applications.* Cambridge, U.K.: Elsevier, 2015.

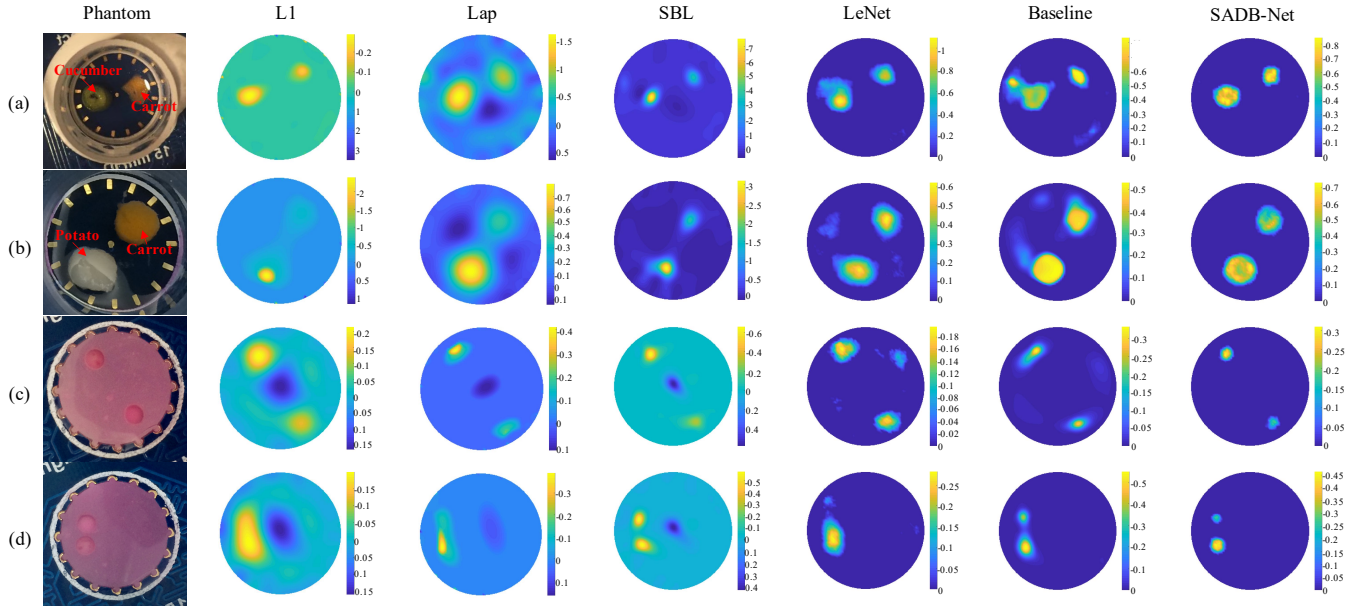

Fig. 9. Experimental results on miniature EIT sensors. (a) Experiment phantom 1: cucumber and carrot cylinders. (b) Experiment phantom 2: potato and carrot cylinders. (c)-(d) Experiment phantom 3 and 4: two MCF-7 cell spheroids.

[3] X. Deng, Y. Chen, Z. Yan, and Z. Wei, "AC impedance model of array electrodes in multisensor fusion system for two-phase flow measurement," *IEEE Trans. Instrum. Meas.,* vol. 59, no. 6, pp. 1722–1726, Jun. 2010.

[4] B. Schullcke, B. Gong, S. Krueger-Ziolek, M. Soleimani, U. Mueller-Lisse, and K. Moeller, "Structural-functional lung imaging using a combined CT-EIT and a Discrete Cosine Transformation reconstruction method," *Sci. Rep.*, vol. 6, pp. 25951, May. 2016.

[5] Y. Yang, J. Jia, S. Smith, N. Jamil, W. Gamal, and P. O. Bagnaninchi, "A miniature electrical impedance tomography sensor and 3-D image reconstruction for cell imaging," *IEEE Sensors J.*, vol. 17, no. 2, pp. 514—523, Jan. 2017.

[6] H. Wu, Y. Yang, P. O. Bagnaninchi, and J. Jia, "Electrical impedance tomography for real-time and label-free cellular viability assays of 3D tumour spheroids," *Analyst.*, vol. 143, no. 17, pp. 4189–4198, 2018. DOI: 10.1039/C8AN00729B.

[7] Y. Yang, H. Wu, J. Jia, P. O. Bagnaninchi, "Scaffold-based 3-D Cell Culture Imaging Using a Miniature Electrical Impedance Tomography Sensor." *IEEE Sensors J.*, vol. 19, no. 20, pp. 9071—9080, Jun. 2019.

[8] Y. Lu, B. Zhu, C. Darne, I. C. Tan, J. C. Rasmussen, and E. M. Sevick-Muraca, "Improvement of fluorescence-enhanced optical tomography with improved optical filtering and accurate model-based reconstruction algorithms," *J. Biomed. Opt.,* vol. 16, no. 12, p. 126002, 2011.

[9] M. Lukaschewitsch, P. Maass, and M. Pidcock, "Tikhonov regularization for electrical impedance tomography on unbounded domains," *Inverse Problems*, vol. 19, no. 3, p. 585, 2003.

[10] A. Borsic, B. M. Graham, A. Adler, and W. Lionheart, "In vivo impedance imaging with total variation regularization," *IEEE Trans. Med. Imag.*, vol. 29, no. 1, pp. 44–54, Jan. 2010.

[11] B. Jin, T. Khan, and P. Maass, "A reconstruction algorithm for electrical impedance tomography based on sparsity regularization," *Int. J. Numer. Methods Eng.*, vol. 89, no. 3, pp. 337–353, 2012.

[12] Y. Yang and J. Jia, "An image reconstruction algorithm for electrical impedance tomography using adaptive group sparsity constraint," *IEEE Trans. Instrum. Meas.*, vol. 66, no. 9, pp. 2295–2305, Sep. 2017.

[13] S. Liu, J. Jia, Y. D. Zhang, and Y. Yang, "Image reconstruction in electrical impedance tomography based on structure-aware sparse Bayesian learning," *IEEE Trans. Med. Imag.*, vol. 37, no. 9, pp. 2090–2102, Sep. 2018.

[14] S. Liu, H. Wu, Y. Huang, Y. Yang, and J. Jia, "Accelerated structure-aware sparse Bayesian learning for three-dimensional electrical impedance tomography," *IEEE Trans. Ind. Inf.*, vol. 15, no. 9, pp. 5033–5041, Sept. 2019.

[15] C. Tan, S. H. Lv, F. Dong, and M. Takei, "Image reconstruction based on convolutional neural network for electrical resistance tomography," *IEEE Sensors J.*, vol. 19, no. 1, pp. 196–204, Jan. 2019.

[16] Z. Chen, Y. Yang, J. Jia, and P. Bagnaninchi, "Deep Learning Based Cell Imaging with Electrical Impedance Tomography," in *Proc. IEEE T. Instrum. Meas.*, Dubrovnik, Croatia, 2020.

[17] J. Ren, Y. Wang, G. H. Liang, and F. Dong, "A Two-Stage Deep Learning Method for Robust Shape Reconstruction with Electrical Impedance Tomography," *IEEE Trans. Instrum. Meas.,* vol. 69, no. 7, pp. 4887–4897, Jul. 2020.

[18] Duan, X., S. Taurand, and M. Soleimani, "Artificial skin through super-sensing method and electrical impedance data from conductive fabric with aid of deep learning," *Scientific Reports,* vol. 9, no. 1, pp. 8831, 2019.

[19] O. Ronneberger, P. Fischer, and T. Brox, "U-net: Convolutional networks for biomedical image segmentation," in *Proc. Med. Image Comput. Comput.-Assisted Intervention*, 2015, pp. 234–241.

[20] S. J. Hamilton and A. Hauptmann, "Deep D-bar: Real-time electrical impedance tomography imaging with deep neural networks," *IEEE Trans. Med. Imag.,* vol. 37, no. 10, pp. 2367–2377, Oct. 2018.

[21] Z. Wei, D. Liu, and X. Chen, "Dominant-current deep learning scheme for electrical impedance tomography," *IEEE Trans. Biomed. Eng.,* vol. 66, no. 9, pp. 2546–2555, Sep. 2019.

[22] Z. Wei and X. Chen, "Induced-current learning method for nonlinear reconstructions in electrical impedance tomography," *IEEE Trans. Med. Imag.,* vol. 39, no. 5, pp. 1326–1334, Oct. 2019.

[23] Z. Chen, Y. Yang, and P. Bagnaninchi, "Hybrid Learning based Cell Aggregate Imaging with Miniature Electrical Impedance Tomography," *IEEE Trans. Instrum. Meas.,* doi: 10.1109/TIM.2020.3035384.

[24] V. Radu, et al., "Multimodal deep learning for activity and context recognition," in *Proc. ACM IMWUT*, vol. 1, no. 4, pp. 157, 2018.

[25] K. S. Cheng, D. Isaacson, J. C. Newell, and D. G. Gisser, "Electrode models for electric current computed tomography," *IEEE Trans. Biomed. Eng.,* vol. 36, pp. 918–924, 1989.

[26] J. Ngiam, A. Khosla, M. Kim, J. Nam, H. Lee, and A. Ng, "Multimodal deep learning," In *Proc. 28th Int. Conf. Mach. Learn. (ICML),* Bellevue, WA,USA, 2011.

[27] N. Audebert, B. L. Saux, and S. Lefvre, "Beyond RGB: Very high resolution urban remote sensing with multimodal deep networks," *ISPRS J. Photogrammetry Remote Sens.,* vol. 140, pp. 20–32, June 2018.

[28] V. Nair and G. E. Hinton, "Rectified linear units improve restricted boltzmann machines," in *Proc. 27th Int. Conf. Mach. Learn. (ICML),*, pp. 807–814, 2010.

[29] J. Johnson, A. Alahi, and L. Fei-Fei, "Perceptual losses for real-time style transfer and super-resolution," in *European Conference on Computer Vision (ECCV), Springer*, pp. 694–711, 2016, doi: https://arxiv.org/abs/1603.08155.

[30] D. Luvizon, D. Picard, and H. Tabia, "Multi-task Deep Learning for

Real-Time 3D Human Pose Estimation and Action Recognition," *IEEE Trans. Pattern Anal. Mach. Intell.*, 2020.

[31] B. H. Brown and A. D. Seagar, "The Sheffield data collection system," *Clin. Phys. Physiol. Meas.,* vol. 8, no. 4A, p. 91, Nov. 1987.

[32] D. P. Kingma and J. L. Ba, "Adam: A method for stochastic optimization," in *Proc. Int. Conf. Learn. Represent.*, 2015, pp. 1–41.

[33] Y. Yang, J. Jia, S. Smith, N. Jamil, W. Gamal and P. Bagnaninchi, "A Miniature Electrical Impedance Tomography Sensor and 3-D Image Reconstruction for Cell Imaging," *IEEE Sensors Journal*, vol. 17, no. 2, pp. 514-523, 15 Jan.15, 2017, doi: 10.1109/JSEN.2016.2631263.

[34] E. Malone, G. S. dos Santos, D. Holder, and S. Arridge, "Multifrequency electrical impedance tomography using spectral constraints," *IEEE Trans. Med. Imag.,* vol. 33, no. 2, pp. 340–350, 2014

[35] Y. Yang, J. Jia, N. Polydorides, and H. McCann, "Effect of structured packing on EIT image reconstruction," in *Proc. IEEE Int. Conf. Imag. Syst. Techn.,* Sep. 2014, pp. 53–58.

[36] K. He, G. Gkioxari, P. Dollar, and R. Girshick, "Mask R-CNN," in *Proc. IEEE Int. Conf. Comput. Vis.,* 2017, pp. 2980–2988.

[37] Y. Yang, H. Wu, and J. Jia, "Quasi-2D EIT-optical Dual Modality Sensor for Cellular Imaging," ELECTRICAL IMPEDANCE TOMOGRAPHY., 2018.